TEKTONIKA

Impact of Material Strength on Releasing Bend Evolution

Alana M. Gabriel *[1], **Hanna M. Elston** [1],
Michele L. Cooke [1], **Christ F. Ramos Sánchez** [1]

[1]Earth, Geographic and Climate Sciences, University of Massachusetts Amherst, USA

Abstract Releasing bends along active strike-slip faults display a range of fault patterns that may depend on crustal strength. Scaled physical experiments allow us to directly document the evolution of established releasing bend systems under differing strength conditions. Here, we use a split-box apparatus filled with wet clay of differing strengths to run and analyze releasing bend evolution. Precut vertical discontinuities within the clay slip with right-lateral displacement of the basal plate followed by the development of oblique-slip secondary faults. In contrast to the weaker clay experiment, which produces left-lateral cross faults that facilitate major reorganization of the primary slip pathway, the stronger clay experiment produces negligible cross faults and has a persistent primary slip pathway. Within both experiments, the dip of initially vertical faults shallows due to lateral flow at depth and left-lateral slip develops along normal fault segments that have highly oblique strike. The experiments show that fault systems within weaker strength materials produce greater delocalization of faulting, with both greater number of faults and greater off-fault deformation that can impact hazard. For example, the hot, thin and weak crust hosting the Brawley Seismic Zone accommodates slip along many distributed faults, which is in sharp contrast to the more localized fault network of the Southern Gar Basin in cooler, thicker and stronger crust. The fault patterns observed in the experiments match patterns of crustal examples and may guide future models of fault evolution within areas of relatively strong and weak crust that have differing heat flux and thickness.

Executive Editor:
Graeme Eagles
Associate Editor:
Hongdan Deng
Technical Editor:
Mohamed Gouiza

Reviewers:
Jürgen Adam
Tim Dooley
Jakub Fedorik

Submitted:
12 May 2024
Accepted:
7 April 2025
Published:
12 May 2025

1 Introduction

Disconnected steps and connected bends along otherwise straight strike slip faults serve as locations of geometrical complexity (e.g., *Mann*, 2007; *Sylvester*, 1988) that can impact the distribution of deformation and the size of damaging earthquakes (*Biasi and Wesnousky*, 2016; *Douilly*, 2023; *Graymer et al.*, 2007; *Ozawa et al.*, 2023; *Wesnousky*, 2006). Ground rupturing earthquakes that propagate along strike-slip faults have greater likelihood of terminating at bends with larger stepover offset, larger bend angle (*Biasi and Wesnousky*, 2016, 2017; *Ozawa et al.*, 2023; *Wang et al.*, 2020; *Wesnousky*, 2006) and topographic contrast across the fault (*Douilly*, 2023). Releasing bends arise when en-echelon fault segments connect such that strike slip creates localized extension around the bend (e.g., *Mann*, 2007). Due to this local extension, ruptures that pass through releasing bends or stepovers can distribute slip among several active strands and as off-fault strain to produce a wide region of deformation (e.g., *Barka and Kadinsky-Cade*, 1988; *DeLong et al.*, 2015; *Duffy et al.*, 2013). Once formed, releasing bends may evolve such that changes in their active fault structure may alter their potential to host large earthquakes.

Whether strain within releasing bends and stepovers is localized along a few faults or distributed among many faults depends on previous fault configuration, nature of loading, and material properties. Numerical models and scaled physical experiments using analog materials to simulate crustal deformation demonstrate that the initial orientation of fault structures plays a strong role in subsequent releasing bend or step over evolution (e.g., *Choi et al.*, 2011; *Dooley et al.*, 1999; *Dooley and McClay*, 1997; *Dooley and Schreurs*, 2012; *Hempton and Neher*, 1986; *Mitra and Paul*, 2011; *Rahe et al.*, 1998; *van Wijk et al.*, 2017; *Wang et al.*, 2017; *Xu et al.*, 2023). For example, previous experiments show that shape and internal structure of basin grabens and the development of secondary faults depends strongly on geometry of the releasing bend (Figure 1; *Dooley et al.*, 1999; *Dooley and Schreurs*, 2012; *Mitra and Paul*, 2011; *Xu et al.*, 2023). While most models and experiments load releasing bends with shear via applied velocity parallel to the segments outside of the bend, models with transtensional far-field loading produce more distributed fault networks (*Dooley and Schreurs*, 2012; *Wu et al.*, 2009). So far, the impact of material properties on releasing bend development has only been directly explored in numerical models. For identical initial fault geometry and loading, numerical models of releasing bends within more viscous materials

---

*✉ alana.gabriel16@gmail.com

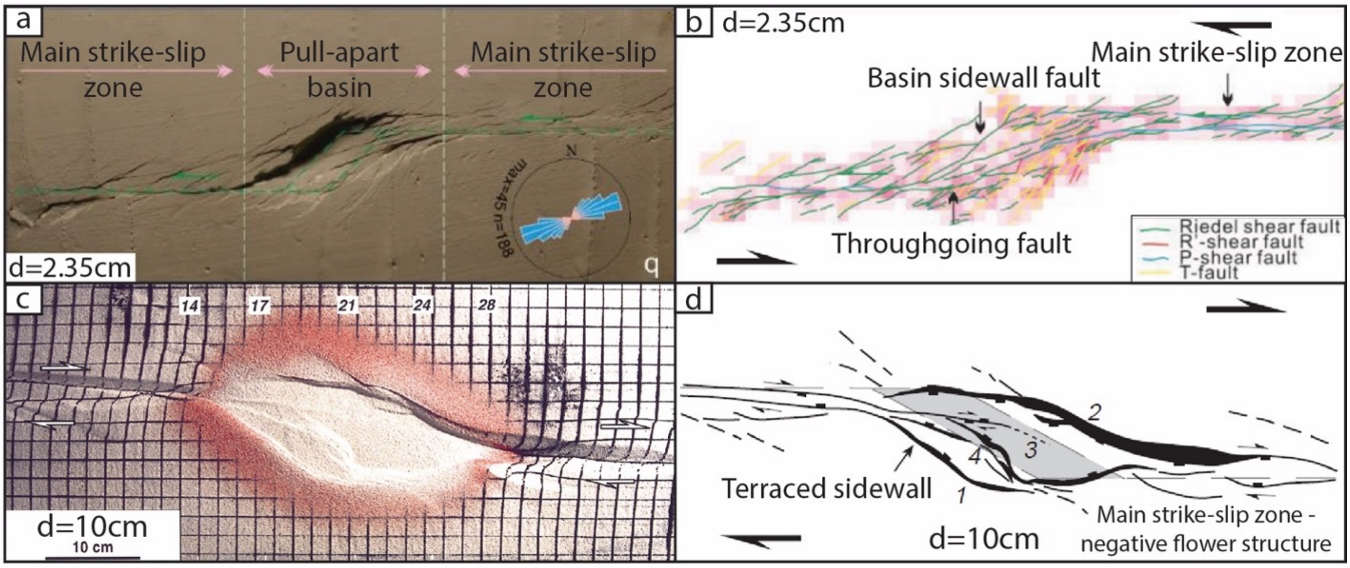

Figure 1 – Examples of previous 30° releasing bend experiments in clay (a and b modified from *Xu et al.*, 2023) and sand (c and d modified from *Dooley and McClay*, 1997). **a)** Overhead photograph of left-lateral releasing bend sketched in **b**. The darkness of the pink squares indicates greater fault density. **c)** overhead photograph of right-lateral releasing bend sketched in **d**.

produce more distributed fault networks than models with less viscous materials (*Wang et al.*, 2017); the increase in viscosity lengthens the stress shadows around faults to foster more distal spacing of faults. The numerical models of *Wang et al.* (2017) also suggest that increasing fault strength relative to material strength produces more diffuse deformation due to lesser localized fault slip along the stronger faults. Because fault strength is challenging to estimate in the crust, we need to use laboratory experiments to validate the suggested relationship between the localization of releasing bend faulting and the relative strengths of the material and the faults.

In this study, we perform scaled physical experiments to investigate the evolution of already established releasing bends within wet kaolin clay of two different strengths, controlled by water content. Kaolin has benefit over granular materials because the strength can be modified by adjusting water content and the established releasing bend faults can be cut into the clay (e.g., *Eisenstadt and Sims*, 2005). By starting the experiments with identical established releasing bends within different strength clay we isolate the impact of material strength on subsequent fault evolution at the geometric irregularities along strike-slip faults. We use Digital Image Correlation tools to track the details of active fault evolution and quantify the strain that drives fault growth. This quantitative analysis of fault kinematics provides an advancement upon previous releasing bend experiments (e.g., *Dooley and Schreurs*, 2012; *Mitra and Paul*, 2011; *Xu et al.*, 2023). We show that the experiments with weaker clay produce a complex network of faults, including arrays of cross-faults with opposing sense of strike slip from the primary faults, whereas stronger material produces fewer, more persistent faults with more localized deformation. The fault networks that develop within the relatively weak and strong clay experiments of this study resemble fault patterns in crustal releasing bends that either developed within thin, hot and consequently relatively weak crust, such as the Brawley Seismic Zone along the San Andreas fault in southern California (USA), or developed in thick, cool and consequently relatively strong crust, such as the Southern Gar Basin along the Karakorum fault in western Tibet.

2 Methods

Scaled physical experiments allow us to simulate the evolution of large crustal faults over millions of years with only hours of lab time using materials that serve as analog for crustal rocks. The experiments allow the direct modification of parameters that can validate proposed controls on fault evolution. To assess the impact of material strength on the evolution of established releasing bends, we analyze the time series of active fault and strain maps from motor-controlled experiments using a split-box apparatus containing wet kaolin clay with two different strengths that simulate differing crustal properties.

2.1 Material Properties and Scaling

The success of the experiments to appropriately replicate upper crustal faulting processes requires the rheology of the crustal analog material to have similar faulting behavior at the scale of the tabletop. The two most commonly used materials for upper crustal deformation studies are dry sand and wet clay (water content > 50%) because the similar frictional behavior to crustal materials and production of faults at low strain facilitates pertinent scaling to the crust (e.g., *Reber et al.*, 2020). Here, we use wet kaolin clay for the releasing bend experiments because the clay allows for the growth of sharp faults that can remain active even when

Table 1 – Experiment material properties.

Experiment	Undrained shear strength	Crustal scaling for 1 cm of clay
Weaker clay	82.2 ± 0.4 Pa	0.8-1.5 km
Stronger clay	110.5 ± 1.3 Pa	0.6-1.1 km

non-optimally oriented (e.g., *Eisenstadt and Sims*, 2005; *Hatem et al.*, 2015; *Withjack and Jamison*, 1986), and we can introduce faults into the material (e.g., *Bonini et al.*, 2023; *Elston et al.*, 2022). Furthermore, we can control the clay strength by adjusting the water content without also changing the frictional properties of the material or faults (*Eisenstadt and Sims*, 2005). The kaolin clay used in the experiments of this study exhibits viscoelastic deformation prior to frictional failure, which appropriately simulates deformation of the upper crust (*Cooke and van der Elst*, 2012; *Reber et al.*, 2020). Previous experiments that simulated faulting using wet kaolin clay produce long-lived fault structures whose evolution and deformation resemble crustal observations of faulting with both strike-slip (e.g., *Elston et al.*, 2022; *Hatem et al.*, 2015, 2017) and extensional regimes (e.g., *Bonini et al.*, 2023; *Henza et al.*, 2010; *Withjack and Jamison*, 1986; *Withjack and Schlische*, 2006).

Using materials that are several orders of magnitude weaker than the crust allows us to simulate crustal deformation within a tabletop apparatus that is several orders of magnitude smaller than the features of interest found in the crust (e.g., *Dooley and Schreurs*, 2012; *Hubbert*, 1937; *Reber et al.*, 2020). We adjust the water content until the clay has the desired undrained shear strength (Table 1), which is measured with a Fall Cone device (*DeGroot and Lunne*, 2007). To estimate the clay:crust length scaling, we follow the analysis of *Hatem et al.* (2015); *Henza et al.* (2010); *Hubbert* (1937) and many others using a clay:crust density ratio of 1.6:2.6 g/cm^3 and a crustal strength range of 10-20 MPa (Table 1). The clay strengths and associated scaling on Table 1 do not represent particular crustal conditions, but both clay conditions with relatively weak and strong values provide reasonable scaling to crustal conditions with 1 cm of the clay representing ∼1 km of the crust. Experiments with drier or wetter clay would produce even greater strength differences, but larger differences in scaling would impede direct comparison of the experimental fault networks. Following *Hatem et al.* (2015) we estimate the water content of the clay prior to and after the experiment. Over the course of each multi-hour experiment in this study, the water content within the upper 1.25 cm of the claypack decreases by less than 3.2% due to evaporation, which correlates to a very small strength increase of less than 4 Pa. The lower half of the claypack does not change water content during the experiment.

2.2 Experiment Setup

Four experiments used a tabletop split-box apparatus filled with either strong or weak wet kaolin clay to record evolution of 30° releasing bends with a 5 cm stepover (Figure 2). The releasing bend geometry represents a sharp bend between two strike-slip faults frequently observed in the crust (e.g., *Mann*, 2007) and simulated in analog experiments (*Dooley and McClay*, 1997; *Mitra and Paul*, 2011; *Xu et al.*, 2023). We present the results from two of the experiments here while details on the second pair of experiments and assessment of the repeatability of the releasing bend evolution can be found in the Supporting Information. The 2.5 cm thick claypack sits on two metal plates that create a basal dislocation with releasing bend geometry similar to previous releasing bend experiments (Figure 2b; *Dooley and McClay*, 1997; *Xu et al.*, 2023). The depth of the experiment base simulates about ∼1-4 km crustal depth and the basal discontinuity applies localized extension and strike slip expected within the upper 5 km of the crust due to deeper faulting. The split box apparatus is controlled by stepper motors that displace the overlying plate with a prescribed velocity of 0.5 mm/min while the underlying plate remains stationary. Because the additional frictional resistance of moving the underlying plate leads to inconsistent stepper motor displacements (*Hatem et al.*, 2015), we displace the overlying plate to yield reliable movement. Restraining bend experiments show that regardless of whether the underlying plate is stationary or moving the fault pattern is similar and the asymmetry of the fault pattern flips with switching of plate stacking (*Hatem et al.*, 2015). All releasing bend experiments had a total displacement of 60 mm.

We investigate the development of established releasing bends so the models may be used as analogs for the subsequent evolution of crustal releasing bends. Prior to the onset of the experiment, we create a vertical discontinuity within the clay pack that follows the basal dislocation with an electrified probe following the approach used for previous faulting experiments (e.g., *Bonini et al.*, 2016, 2023; *Cooke et al.*, 2013; *Elston et al.*, 2022). The breadth of this study excludes the initiation of releasing bends, which, in order to study, we would opt to follow the approach used in previous experiments and leave the claypack uncut (*Dooley et al.*, 1999; *Dooley and McClay*, 1997; *Mitra and Paul*, 2011; *Xu et al.*, 2023). Cutting the entire releasing bend fault prior to the experiments of this study allows us to investigate the evolution of established crustal releasing bends that already have a continuous active strike-slip pathway.

We utilize Digital Image Correlation techniques (e.g., *Adam et al.*, 2005) to extract incremental horizontal displacement fields to define fault maps and calculate strain partitioning. Onto the surface of the clay, we sieved red and black sand that act as texture to aid Digital Image Correlation. To capture both horizontal displacements and vertical elevation, one 24.1 Megapixel DLSR camera with fixed length lens was placed directly above the clay box and the remaining four 24.1 Megapixel DLSR cameras with zoom lenses captured different perspectives of the claybox during the experiment (Figure 2a). Photos from the overhead camera provide images for calculating horizontal displacements using Particle Image Velocimetry while photos from all five cameras were used to capture topographic changes using Structure from Motion. Because the fault system provides greater rates of horizontal movement than vertical movement, we use a faster rate of image capture for the overhead camera, which is used to determine horizontal movements. The overhead camera took photos every 0.25 mm of plate displacement while the remaining cameras took photos every 1.25 mm of plate displacement. We analyze the incremental displacement fields within a region of interest far from the experiment boundaries to avoid boundary effects (Figure 2).

During the experiments, extensional basins formed and exposed fresh clay along normal fault surfaces that lacked sand particles that facilitate the Digital Image Correlation. The lack of texture on the newly exposed fault surfaces introduces local errors in the displacement fields. To reduce these errors along the fault surfaces, we sieved the newly exposed clay with additional sand as needed at 41 mm plate displacement during the weaker clay experiment and at 30 and 47 mm plate displacement during the stronger clay experiment.

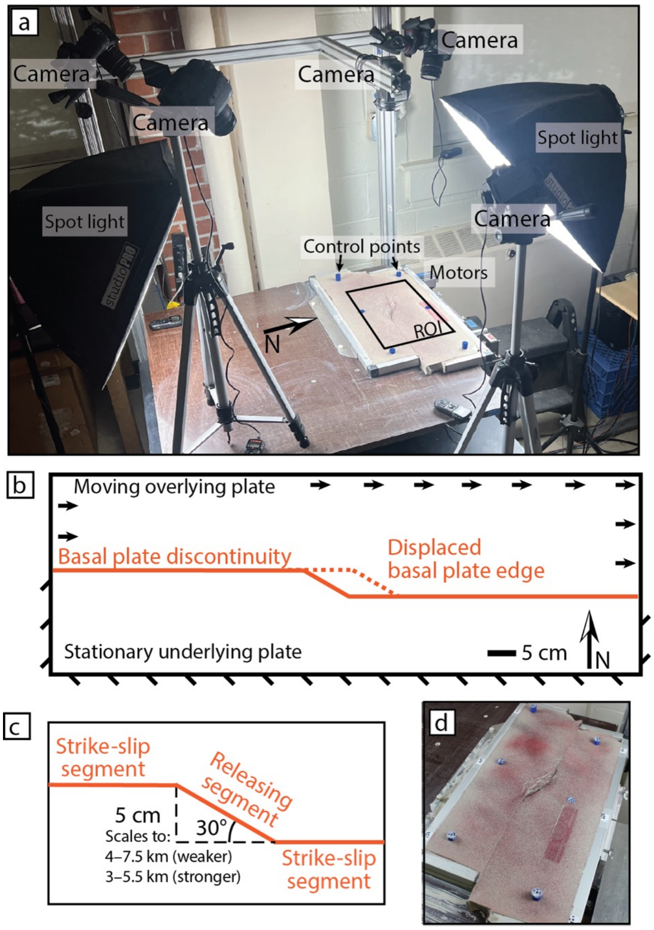

Figure 2 – Experimental setup. **a)** Photograph of the experimental laboratory at UMass Amherst. The black box indicates the region of interest (ROI) the overhead cameras capture. **b)** Top view of the boundary conditions for the ROI shown in a). The solid red line highlights the basal plate discontinuity at the start of the experiment and the dashed line shows the edge of the displaced plate. **c)** Sketch of fault geometry precut into the claypack. **d)** Oblique view of weaker clay experiment at 48 mm plate displacement showing central graben with many normal fault scarps and the experimental apparatus.

2.3 Digital Image Correlation and Photogrammetry Techniques

Particle Image Velocimetry calculates horizontal incremental displacement fields on the surface of the claypack from successive image pairs of the claypack surface. The Matlab^{TM} tool, PIVlab (*Thielicke and Sonntag*, 2021) tracks the displacement of unique configurations of sand particles between successive photos. In this analysis, a three-pass Fast Fourier Transform filter yields incremental displacement values every 0.49 and 0.5 mm for the stronger and weaker experiments respectively. To reduce noise from the incremental displacement fields, we apply a 5-point (~6.25 mm^2) median filter that does not impact the width of localized strain zones. The vorticity of the incremental displacement fields reveals the incremental shear strain, and the divergence reveals the incremental dilation within the system. Because the divergence values are generally low in this system that has applied right-lateral loading, we also stack the divergence over five incremental displacement maps to reduce noise. We use the sum of the two strain fields to map active faults and calculate slip partitioning. The addition of sand on freshly exposed clay partway through the experiments introduced an abrupt change to the surface that cannot produce reliable incremental displacement fields across that interval. These select displacement fields impacted by the addition of sand were removed from subsequent analysis.

To capture the clay surface topography at chosen plate displacements during both experiments, we use the Structure from Motion software, Metashape^{TM}. Structure from Motion uses multiple images and the known position and elevation of ground control points to develop a three-dimensional point cloud of the surface (e.g., *Bonali et al.*, 2019; *Galland et al.*, 2016; *von Hagke et al.*, 2019). We use images from all five cameras and 12 ground control points; six inside and six outside of the box. Within the box we placed six lightweight three-dimensional cylinders with similar diameter and differing heights (2-22 mm) on the surface of the wet kaolin without perturbing the region of potential faulting (Figure 2). Six permanent one-dimensional control points located on the edges of the split box apparatus also constrain the point cloud development (Figure 2d). Considering that net uplift and subsidence from dip slip along faults and off-fault deformation is on the order of several millimeters, the < 0.5 mm uncertainty of elevation estimates produced using Structure from Motion (see Supporting Information) is within our metrological error budget. We collected topographic data at 60 mm plate displacement when normal slip along the precut releasing segments and secondary faults produced basin subsidence. The elevation information provides a direct way to characterize the basin geometry.

2.4 Active Fault Network Deformation

The times series of incremental strain fields reveal the evolution of both localized slip along faults and distributed strain throughout the experiments. To assess the degree of on and off-fault deformation we develop active fault maps at every 0.25 mm of plate displacement through the experiment using an adaptive threshold technique to detect regions of localized net incremental strain ($|\Delta vorticity| + |\Delta divergence|$). This approach performs well at detecting localized faulting within regions of both high and low background strain (*Chaipornkaew et al.*, 2022). To reduce noise in the net strain maps prior to fault detection, we stack seven frames of the strain time series, which corresponds to $\sim$ 1.75 mm of applied basal plate displacement. The adaptive threshold assesses strain localization within a neighborhood size of 9 by 9 pixels (4.5 x 4.5 mm), with 0.01 sensitivity and we filter out regions of very low net incremental strain (average incremental net strain in the neighborhood is < 0.005). This serves to remove small fault regions of higher than background strain with <8 connected pixels, equivalent to ∼5 mm long faults.

Releasing bends within experiments of different clay strength may exhibit different degrees of off-fault deformation, which can inform our expectations for strain partitioning within crustal releasing bends. To assess the capacity of the fault system to accommodate the applied loading as fault slip, we calculate the kinematic efficiency of the fault system. Kinematic efficiency is defined as the ratio of fault slip rate (in the direction of loading) to the applied velocity of 0.5mm/min. Efficient fault systems have greater fault slip and lesser off-fault deformation. Very early in experiments, prior to the spin up of slip along the precut fault, strain is distributed and kinematic efficiency is zero. As faults evolve within experiments, the kinematic efficiency increases and may approach one as the total fault slip rate parallel to loading across all the faults nears the applied velocity (e.g., *Hatem et al.*, 2017; *Chaipornkaew et al.*, 2022). We calculate kinematic efficiency by summing the fault slip component parallel to applied loading for all faults along transects perpendicular to the applied velocity. Within some parts of the system, such as within the releasing bend, the kinematic efficiency may be lower (greater off-fault strain) than outside of the bend, where faults strike parallel to the loading. For the analysis here, we find the overall kinematic efficiency within the region of the experiment that contains new fault growth and exclude from the analysis areas farther than 49 mm from either of the two kinks of the migrating basal plate releasing bend (185 mm total length of analysis region). With movement of the basal plate during the experiment, the region of new faulting migrates relative to the camera, and we adjust the position of the analysis region based on this advection; we do not change its size. We use this same analysis region to assess the amount of divergence accommodated along faults (i.e., dip slip) within each experiment.

The overall kinematic efficiency and divergence within the analysis region inform how strain is accommodated on and off of faults. To determine the overall kinematic efficiency of the fault system, we take the median of measurements along 398 transects that cross the faults within the analysis region. The maximum, minimum and standard deviation of the kinematic efficiency measurements on the transects reveal the spatial variation of localized slip along the fault system. We note that this overall kinematic efficiency doesn't track whether individual faults have right- or left-lateral slip but assesses the overall impact of the fault system to accommodate the applied right-lateral shear. To assess the partitioning of divergence as either dip slip along faults of any orientation or distributed off-fault extension, we calculate the median of the divergence accommodated along faults that is measured along transects within the analysis region.

3 Fault Evolution

Here, we describe the fault system evolution for experiments following the initiation of slip along the entire precut releasing bend referred to as the spin-up period (Figures 3, 4 and 5). While data from the spin-up period is included in some figures, our analysis focuses on the reorganization of established releasing bends. After the spin up period of ∼5 mm of basal plate displacement, all portions of the precut fault slipped, and the ensuing experimental deformation simulates long-term deformation of active crustal faults that have a releasing bend structure. Both experiments developed secondary normal faults that produced a basin within the releasing bend. For each of the experiments, we distinguish two stages of fault development that characterize 1) initial growth of new normal faults, 2) reorganization of the primary slip pathway through the releasing bend. While the fault evolution stages in each experiment have similarities, the two experiments with different clay strength grow fault networks with differing degrees of complexity and strain localization (Figures 3, 4 and 5).

3.1 Stronger Clay Experiment

The initiation, growth and linkage of new secondary faults characterize stage one of the stronger clay experiment (Figures 3a-d and 4a). We delineate early stage one (stage 1a) when many new faults developed from late stage one (stage 1b) when slip patterns evolved without new fault growth. Stage 2 started when the slip along the precut slip pathway shifted onto new faults (see strain animations from *Gabriel et al.*, 2025).

3.1.1 Stage 1a (9-30 mm plate displacement)

Most new secondary faults grew during stage 1a as normal faults that trended subparallel to the releasing segment and accommodated primarily extensional deformation (+divergence; Figure 3a-c). About half of the new secondary faults initiated along the precut fault (Figure 3a-c; Figure 4). The secondary faults lengthened

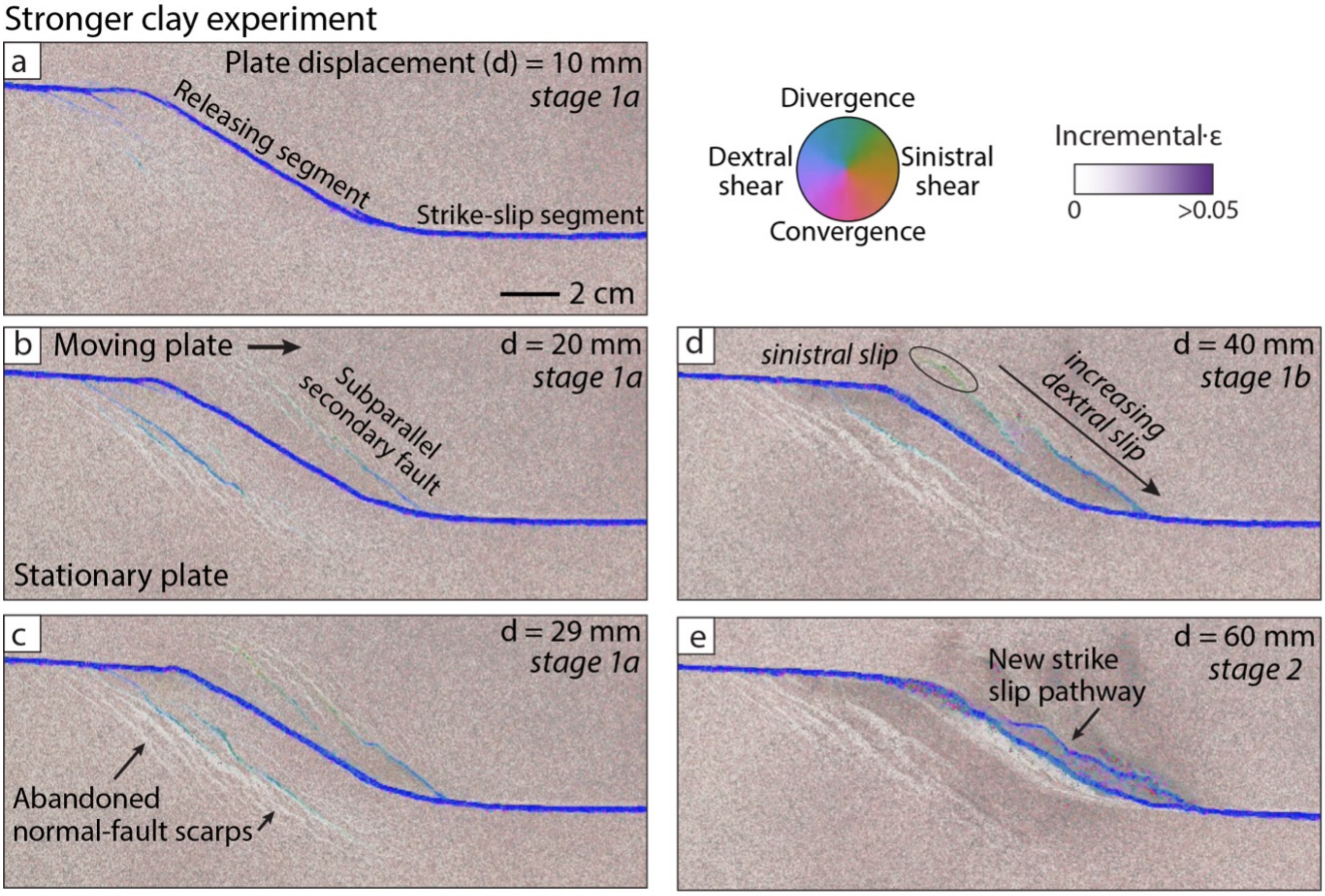

Figure 3 – Incremental strain maps for stronger clay experiment overlain on images of the experiment surface at 10, 20, 29, 40 and 60 mm of plate displacement. Saturation indicates incremental strain magnitude and hue indicates sense of strain.

by both propagation and by linkage with other small faults. The slip sense varied spatially along the normal faults with greater component of right-lateral strike slip where they connect to the precut faults (Figure 3b-c).

While the photographs show many fault scarps in the clay on both sides of the releasing bend, only one or two on each side were concurrently active (Figure 3b-c). The incremental strain shows that active slip on these normal faults successively shifted onto new faults that developed nearer to the precut releasing segment and basinward (Figure 3b-c). With the basinward shift in fault activity, fault segments further from the precut releasing segment ceased slipping. This shift produced a pattern of faults that younged towards the basin.

The number of active secondary normal faults decreased during stage 1a. While five faults were active at 13 mm of plate displacement above the stationary plate, by 34 mm of plate displacement only one fault was active. At the end of 1a (30 mm plate displacement), two secondary faults were active above the stationary plate. Figure 3c highlights many small scarps created by previously active normal faults.

3.1.2 Stage 1b (30-49 mm plate displacement)

During the late part of stage 1 (stage 1b), the active slip was partitioned among only a few faults, and no new secondary faults initiated (Figure 3d and e). After 30 mm of plate displacement, the remaining secondary fault above the stationary plate accommodated decreasing oblique right-lateral and extensional strain (Figure 3d) until it ceased slipping before the end of stage 1 (39 mm of plate displacement). In contrast, the two active secondary faults above the moving basal plate accommodated greater incremental strain during stage 1b and exhibited spatially heterogeneous combinations of right-lateral shear, extension and left-lateral shear at different locations along the fault (Figure 3d). Throughout stage 1b, portions of faults above the moving plate closest to the precut fault displayed greater right-lateral slip than segments further to the northwest (Figure 3d). The most northwestern normal faults showed small components of left-lateral slip (Figure 3d). The sand-free scarps in the overhead photograph of Figure 3d confirm significant dip slip along the normal faults determined from the sense of the incremental strain fields.

3.1.3 Stage 2 (49-60mm plate displacement)

During stage 2 of the stronger experiment, the primary right-lateral slip pathway reorganized to include portions of the secondary faults (Figure 3e). At the beginning of stage 2, the two active secondary faults linked up to form a single fault by ∼53 mm plate displacement. With increasing plate displacement, the portion of the

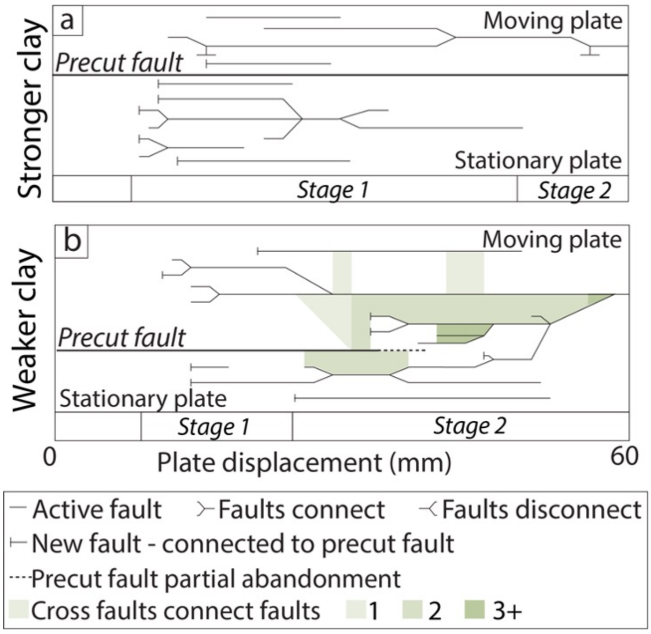

Figure 4 – Fault evolution timelines for **a)** stronger and **b)** weaker clay experiments. Each line represents the active period of a fault. The line caps represent direct connection to the precut fault. Lines below and above the bold precut fault line represent faults that develop over the stationary and moving plates respectively. Where lines connect, the faults linked in the experiment. Faults connected by cross-faults are bound green regions of the timeline for the weaker clay experiment. Comparison of the experimental timelines reveals differences of releasing bend evolution within materials of different strength. The greater number of faults active in the weaker clay experiment is represented by the combination of black lines and green shading (cross faults). The weaker clay experiment timeline also shows the abandonment of the precut fault during stage 2.

fault, which had a component of left-lateral slip, ceased slipping and the portion of the secondary fault that remained active propagated westward to link with the precut fault (Figure 3e). With that linkage, the releasing bend had a second continuous pathway for right-lateral slip through the releasing bend (Figure 3e). The incremental strain accommodated along the new slip pathway increased with its connection to the precut fault at ∼58 mm of plate displacement. Both slip pathways through the releasing bend accommodated both right-lateral slip and extension and bound a graben located above the moving plate (Figures 3e and S1 in Supporting Information). The preference of new slip pathway and graben development over the moving plate owes to the asymmetry in the motion of the basal plates. Restraining bend experiments document similar asymmetry that flips when the moving plate underlies the stationary plate (*Hatem et al.*, 2015). The overhead photograph of Figure 3e reveals sand-free scarps along the initially vertical precut releasing segment indicating that this surface developed dip slip and is no longer vertical by the end of the experiment.

3.2 Weaker Clay Experiment

3.2.1 Stage 1 (8-25 mm plate displacement)

The initiation, growth and linkage of secondary faults characterized the first stage of the weaker clay experiment (Figure 5a). Similarly to the stronger clay experiment, early normal faults formed on both sides of the releasing bend that trend parallel to the precut releasing fault segment (Figure 5a-c). Some of the new secondary faults grew from the precut fault, while other secondary faults initiated away from the precut fault (Figure 4; Figure 5a-c). The faults initiated with primarily normal slip with segments nearer to the precut fault having greater component of right-lateral slip (Figure 5a-c). During stage 1, most of the secondary faults linked up with one another, and only one secondary normal fault ceased slipping during this stage (Figure 4). Throughout stage 1, the faults above the moving plate accommodated increasing incremental strain (Figure 5a-b). The most northwestern portions of these faults showed a small component of left-lateral slip where the faults curve, similarly to the faults of the stronger experiment (Figures 3a-c and 5a-b).

3.2.2 Stage 2 (25-60 mm plate displacement)

In the weaker clay experiment, the reorganization of the primary slip pathway started at lower plate displacement than within the stronger experiment and was accompanied by the initiation of new left-lateral cross faults that trended at high angles to the precut releasing segment (Figure 5c-e). The cross faults connected the releasing segment to the secondary faults that grew during stage 1 (Figure 5c-e). While the secondary faults continued to accommodate primarily right-lateral shear and extension, the cross faults accommodated left-lateral shear and extension. In addition to cross faults, new secondary faults with trends subparallel to the precut releasing segment continued to initiate throughout the second stage (Figure 5c-e). Many new secondary faults grew between cross faults and connected with other secondary faults creating an evolving complex ladder-like pattern of active faults (Figure 5c-e).

At the beginning of stage 2, the precut fault accommodated primarily right-lateral shear and provided the only throughgoing pathway for strike slip. However, by ∼32 mm of plate displacement, the southern portion of the precut releasing segment ceased slipping as a secondary fault linked with the precut releasing segment to form a straighter pathway for right-lateral slip (Figure 5c). Similarly to the experiment with stronger material, the new slip pathway and the graben that forms between it at the precut fault surface preferentially develop over the moving plate (Figures 5c and S2 in Supporting Information) due to the asymmetry of the applied basal loading. By ∼39 mm of plate displacement, other secondary faults had linked to the precut fault in the northern region to create a new continuous and through-going pathway for slip. With the development of this new slip pathway, slip

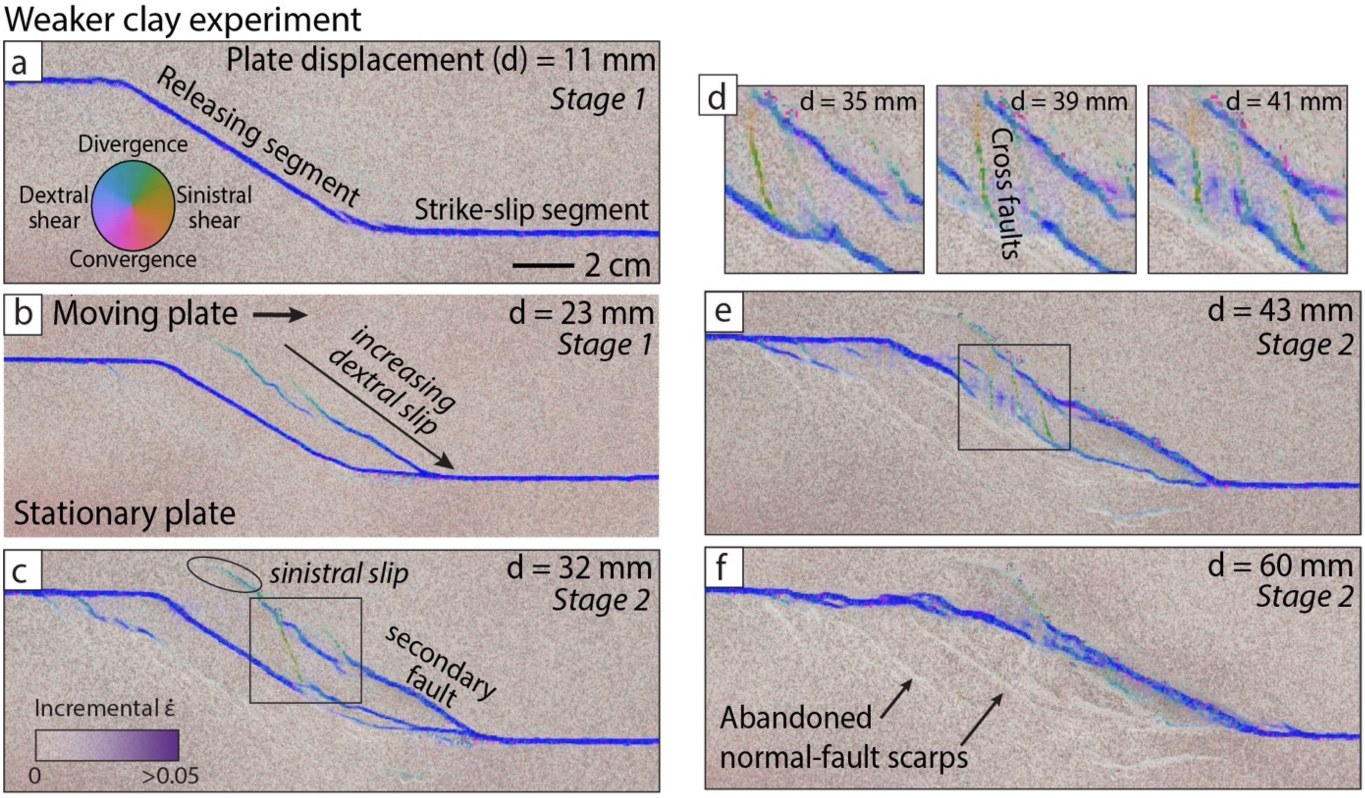

Figure 5 – a-c, e and f) Incremental strain maps for the weaker clay experiment overlain on images of the experiment surface at 11, 23, 32, 43 and 60 mm of placement displacement. Saturation indicates incremental strain magnitude and hue indicates sense of strain. **d)** Incremental strain maps overlain on images of the clay surface at 35, 39, and 41 mm of plate displacement for the regions indicated by the rectangles in c and e that show cross-fault development.

ceased along all portions of the original precut releasing segment; the precut strike-slip segments outside of the bend remain active. Figure 5 (e and f) shows scarps along the abandoned precut fault surface indicating that this fault was no longer vertical by stage 2 of the weaker clay experiment.

The overall orientation and position of the ladder-like zone of active faults in stage 2 of the weaker experiment mimics the releasing bend discontinuity of the underlying basal plates. The new secondary faults that parallel the releasing bend accommodated right-lateral slip and a greater component of extension than the precut fault in stage 1 (Figure 5c-e). During stage 2, faults to the west were successively abandoned in favor of new faults to the east until only a single releasing segment persisted at the end of this stage (Figure 5f). After 30 mm plate displacement, the cross faults continued to connect the secondary faults and experienced clockwise rotation, which is highlighted in Figure 5d. While the cross-faults trended northwest-southeast at ∼30 mm plate displacement, they trended north-south by 47 mm plate displacement (Figure 5e). At the end of the experiment, activity on cross faults ceased as slip localized along one releasing bend fault (Figure 5f).

4 Active Fault Network Deformation

To investigate how strain is accommodated along the fault network, we examine the evolution of both the divergent strain accommodated along the active fault system (i.e., dip slip) and the kinematic efficiency. The kinematic efficiency sums the component of fault slip parallel to the applied displacement, which can be a component of strike slip if the faults trend oblique to the loading.

4.1 Divergence Accommodated (Dip Slip) along Faults

The overall accommodation of divergence as dip slip on faults increases significantly with releasing bend evolution during both experiments. After the spin-up period, both experiments show a gradual increase in incremental divergence accommodated by normal slip along faults (Figures 3a-c, 5a-b and 6a-b). During stage 1, the divergence is primarily accommodated along secondary faults rather than the precut fault (Figures 3a-c and 5a-b). In both experiments, the dip of the precut releasing segment shallowed during stage 2 allowing the precut fault to accommodate greater dip slip (Figures 3 and 5). Consequently, divergence during stage 2 was accommodated as dip slip along both the precut fault and secondary faults.

Both experiments show episodes of lesser and greater

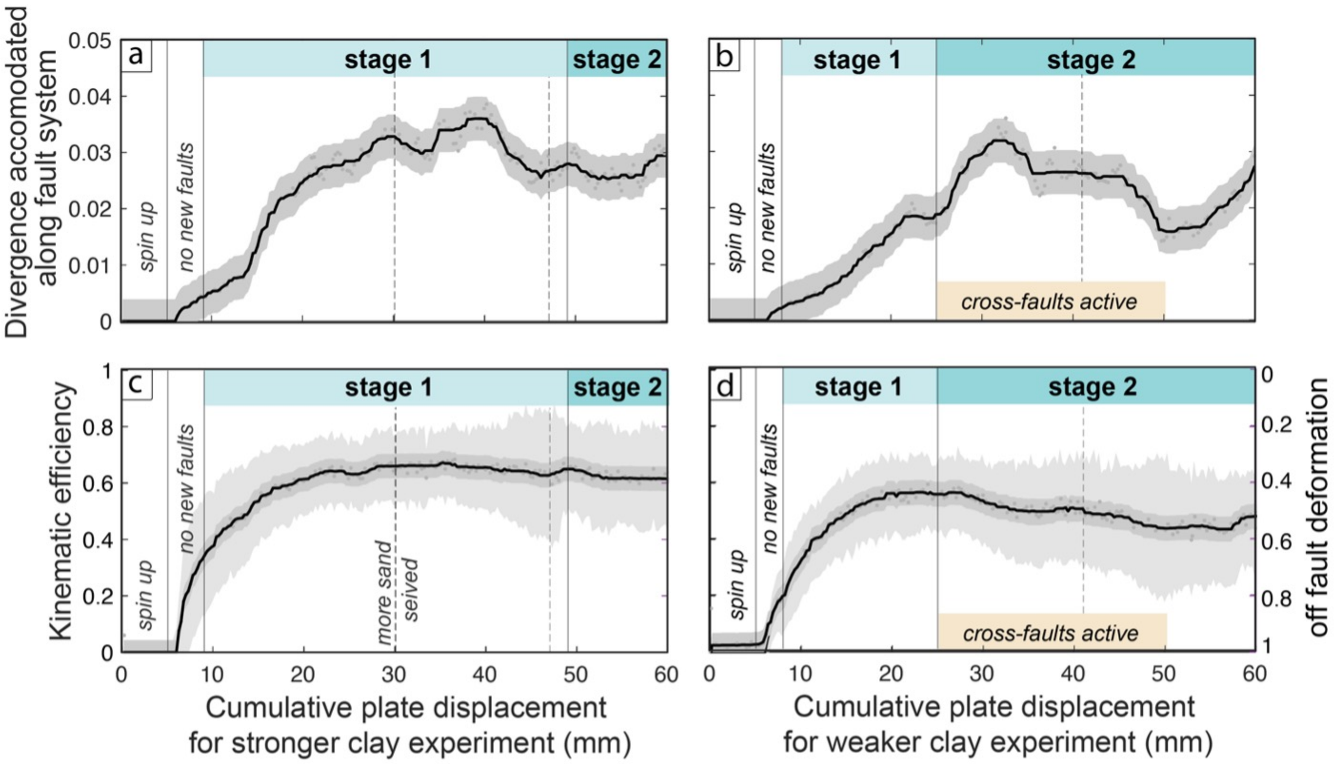

Figure 6 – The bold line represents the overall **a and b)** divergence accommodated along or **c and d)** kinematic efficiency of the active faults within the experiments. The releasing bend fault segment, all secondary faults, and 49 mm of the main strike-slip faults on either side of the releasing bends are included in the fault system represented in the figures. The dark grey region represents the bounds of one standard deviation from the median of values calculated from 398 north-south transects across the analysis region. The lighter grey for the kinematic efficiency shows the minimum and maximum values of all the transects. Dashed lines indicate when additional sand was sieved onto the clay surface to enhance DIC analysis on the newly exposed clay along normal fault surfaces.

degree of dip slip along the faults within the releasing bend (Figure 6a and b). The stronger experiment had two episodes of decreased accommodation of divergence around 30 mm and 40 mm plate displacement during stage 1 (Figure 6a). These episodes are associated with both the abandonment of dip-slip secondary faults and the shift of slip sense on the portion of secondary fault connected to the precut fault to greater strike slip and lesser dip slip (Figures 3 and 5). Within the weaker clay experiment, faults accommodated the maximum divergence during stage 2 at ∼33 mm basal plate displacement. From 32 mm to 36 mm plate displacement, the dip slip along faults decreased (Figure 6b) when secondary faults linked with the precut fault and reconfigured the primary strike-slip pathway. The dip slip along faults dropped again after ∼46 mm plate displacement (Figure 6b) with another reconfiguration of the primary strike-slip pathway that also disrupted slip along the cross faults that had been accommodating a component of divergence (Figure 5d-e). At the end of both experiments the releasing bend fault systems accommodated increased dip slip after the reorganization(s) of the primary slip pathways (Figure 6a and b).

4.2 Kinematic Efficiency of the Fault Systems

Within both experiments, the kinematic efficiency generally increased as the slip rates along the evolving fault network increased, and the faults accommodated an increasing portion of the applied loading. Prior to the growth of new faults, 20-30% of the applied deformation was accommodated as slip along the precut fault surfaces with greater slip in the stronger clay experiment (Figure 6c and d). The weaker experiment had a greater proportion of off-fault deformation prior to any fault growth and for both experiments, the off-fault deformation decreased as new, more efficient faults developed. During stage 1, the fault networks of both experiments reached maximum kinematic efficiency (Figure 6c and d).

Within the stronger clay experiment, the kinematic efficiency reached a steady state in stage 1 that persisted to the end of the experiment despite changes to the configuration of the fault system (Figure 6c). As new, right-lateral normal faults developed, grew and linked in stage 1 of the stronger experiment, the kinematic efficiency rose from 30% to 64% (Figure 6c). The growth of the secondary faults created a more efficient fault system to accommodate deformation. Even though the number of active secondary faults decreased during the later part of stage 1 (Figure 4), the kinematic efficiency remained around 64% throughout stage 1 of the stronger experiment (Figure 6c) suggesting that slip rate increased along the individual faults that persisted. Despite the reorganization of the primary pathway for slip through the releasing bend and other changes to the network, the fault system maintained steady kinematic efficiency and degree of off-fault deformation through the later half of stage 1 and stage 2 (Figure 6).

Within the weaker clay experiment, the kinematic efficiency fluctuated after reaching a maximum during stage 1. With the initiation, growth and linkage of secondary faults during stage 1 of the weaker clay experiment, the kinematic efficiency increased from 20% to 56% (Figure 6d). The emergence of secondary faults with oblique slip provided a more efficient fault network to accommodate the right-lateral loading than the vertical precut releasing bend fault. However, during much of stage 2, which is characterized by reorganization of the primary slip pathway, the kinematic efficiency decreased (Figure 6d). The period of normal and left-lateral slip along cross faults (20 to ∼50 mm of plate displacement; Figure 3) correlates with the period of steady decrease of kinematic efficiency and increase in off-fault deformation (Figure 6d). After 50 mm plate displacement, the kinematic efficiency remained steady and increased slightly after 57 mm plate displacement (Figure 6d). The kinematic efficiency of the weaker clay experiment varied more than that of the stronger clay experiment due to the larger reorganizations of the fault network and primary slip pathways. The lower value of kinematic efficiency of the weaker clay experiments reveals the greater off-fault deformation within the fault system dominated by many active faults and multiple reorganizations of the primary slip pathway.

5 Discussion

The fault zones in the experiments of this study with pre-established releasing bend fault show similar evolution as other releasing bend experiments that inform fault initiation by omitting precut faults (*Dooley et al.*, 1999; *Dooley and McClay*, 1997; *Mitra and Paul*, 2011; *Xu et al.*, 2023) with varied angles, offset distances, loading rates, and material properties. After the activation of slip along precut faults or development of initial throughgoing faults in uncut experiments, the secondary faults grow and connect with other secondary faults during basin development (Figures 1, 3 and 5 stage 1; i.e., *Dooley et al.*, 1999; *Dooley and McClay*, 1997; *Mitra and Paul*, 2011; *Xu et al.*, 2023). Ultimately, experiments form throughgoing slip pathways (*Dooley and McClay*, 1997; *Mitra and Paul*, 2011; *Xu et al.*, 2023). Some experiments, including the 30° releasing bend in the sandpack experiment of *Dooley and McClay* (1997), show the secondary faults connecting to the throughgoing faults to rearrange the throughgoing pathway like we see during stage 2 (figures 3 and 5). Some structures only emerge in a few releasing bend experiments. For example, the 30° releasing bend experiment in *Xu et al.* (2023) develops cross faults at high angle to the releasing segment (Figure 1). Previous experiments carefully document the fault evolution, and the experimental results of this study expand upon this approach by using DIC to reveal strain fields that shed insight into the processes that drive releasing bend fault evolution.

The models presented here show the strength of the clay has a significant impact on fault evolution in releasing bends. While both experiments have initial periods of secondary normal fault growth, the weaker clay experiment developed a greater number of secondary faults and had greater off-fault deformation, which suggests more distributed deformation overall than the stronger clay experiment. Additionally, the stronger clay experiment had a more persistent primary slip pathway that showed only minor reorganization compared to the major reorganizations of primary slip pathway recorded throughout stage 2 in the weaker experiment. The weaker clay experiment also developed cross faults with normal and left-lateral slip, which do not develop in the stronger clay experiment. The overall efficiency decreased with development of the ladder-like fault pattern with opposing strike-slip sense on the uprights (i.e., faults parallel to the releasing segment) and rungs (i.e., cross-faults) of the ladder (Figure 5d-f; Figure 6). The greater off-fault deformation during this period of active cross faulting also facilitated the development of new faults that reorganize the primary slip pathway into a more efficient configuration. Strain accumulating in regions other than on faults can promote failure and the initiation of new faults and/or propagation of existing faults. The weaker clay experiment shows greater variation in fault system efficiency and divergence that correlate with major reorganization of the slip network and associated strain partitioning. Here, we describe the mechanisms that give rise to the features and faulting patterns seen in our experiments.

5.1 Repeatability

To assess the repeatability of fault evolution at releasing bends, we ran a second set of experiments with identical boundary conditions and clay strength values that overlap those of clay in the experiments presented in detail (see Supporting Information). The repeated stronger and weaker clay experiments had similar geometry and timing of fault evolution as the experiments presented here. All four experiments had two clear stages of activity after the spin-up period: 1) growth of new normal faults with right- and left-lateral slip, 2) reorganization of the primary slip pathway through the releasing bend (see Supporting Information for experiment description and *Gabriel et al.* (2025) for animations of the experiments' strain evolution). When comparing the sets of experiments, we note that the stronger clay experiment has simpler active fault geometry with fewer and more persistent active faults compared with the weaker clay experiments. However, the repeated stronger clay experiment showed some differences from the one presented in Figure 3. During the rearrangement of the throughgoing slip pathway in the repeated stronger experiment, a few short-lived cross faults developed. However, the left-lateral cross faults were only active for 2 mm of plate displacement (see Supporting Information), were limited to regions between closely spaced right-lateral faults and were considerably less prominent than in either weaker clay experiments where cross-faults were active for 20-25 mm of plate displacement and contributed to reorganization of the primary slip pathway.

5.2 Changing Fault Dip and Accommodation of Divergence

In both experiments, the precut releasing segment accommodates greater divergence as the dip of the initially vertical fault decreases (i.e., shallows) and the fault accommodates greater normal slip. The shallowing dip and rotation of the precut releasing bend segment can be attributed to lateral flow of the viscoelastic clay at depth within the claypack (Figure 7). At the beginning of the experiment, the clay had uniform thickness above both the stationary and moving plates. As the moving plate displaced, local extension thinned the claypack adjacent to the releasing segment of the precut fault creating a basin on the hangingwall (Figure 7c). Local differences in the claypack thickness create lateral differences in overburden pressure with greater pressure within thicker areas of the claypack. The lateral difference in overburden pressure between the thicker footwall and thinner hangingwall promotes slow, lateral flow of viscoelastic clay from the footwall above the moving plate to the hangingwall on the stationary plate that shallows the fault dip (Figure 7c).

5.3 Slip Sense

Both experiments are loaded with right-lateral shear and develop some faults with shear sense opposite to the applied loading. Here, we explore the processes that contribute to the development of left-lateral slip along faults within this right-lateral system.

5.3.1 Left-lateral Slip along Cross Faults

One of the main differences between the stronger and weaker experiments is the persistent pattern of left-lateral slip along cross faults between right-lateral slip along secondary faults within only the weaker clay experiment. We note that all of these faults have oblique slip vectors, but here we discuss the strike-slip components along the faults. The left-lateral cross faults and the right-lateral secondary faults that trend subparallel to the precut releasing bend segment form a conjugate fault pattern in that they have opposing slip sense and an angular relationship consistent with conjugate fault sets (Figure 8). While right-lateral loading can theoretically produce left-lateral shear on roughly north-south oriented fault structures (Figure 8 inset), significant left-lateral slip along north-south faults only developed in the experiment with the weaker clay. Greater off-fault deformation within the weaker clay experiment contributes to new fault growth. Furthermore, the stronger clay experiment develops fewer, more persistent faults than the weaker experiment. Both the lower strength and greater off-fault deformation of the weak clay experiment promote the growth of new north-south trending cross-faults that link the right-lateral secondary faults. The orientation of the new cross-faults is well-suited to accommodate left-lateral shear under the applied loading (Figure 8). The fault system of cross-faults resemble domino faults where one set of faults (i.e., right-lateral faults) have greater slip and are more prevalent than the other (i.e., left-lateral). *Nixon et al.* (2011) showed that domino fault systems may accommodate greater rotation than systems with equal slip. We also see significant rotation of the cross faults in the weaker clay experiments.

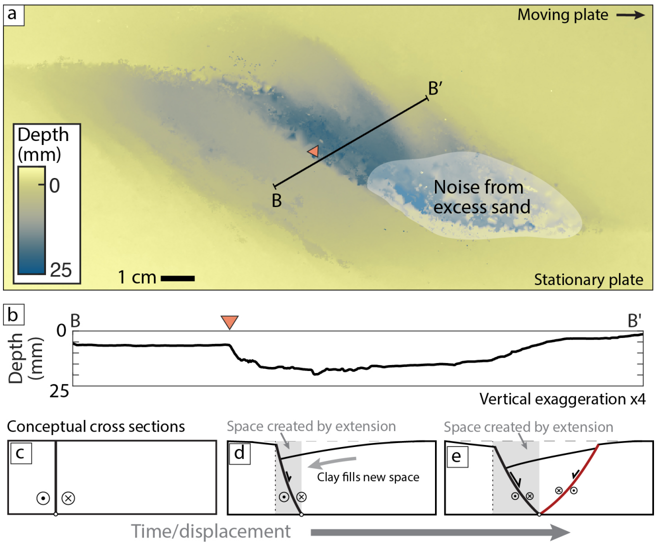

Figure 7 – **a)** Depth map at 60 mm of displacement in the stronger clay experiment. The depth along line B-B' is shown in **b)**. The orange triangle indicates the location of the precut fault along line B-B'. **c-e)** Schematic cross sections showing a simplified progression of faults and the clay surface throughout the experiment along line B-B'. Time in the experiment and applied basal plate displacement increase to the right. The basal plate discontinuity location is indicated by the white circles at the bottom of each panel. Black lines indicate current clay bounds and dashed grey line indicates the initial clay surface. **c)** initial condition – the precut fault (bold black line) is vertical and accommodates dextral shear. **d)** With applied displacement, extension within the restraining bend creates space (grey rectangle). Clay on the moving plate moves away from the stationary plate and the clay at depth flows laterally to fill the new space. This results in a change in the surface topography of the clay. The precut fault shallows in dip with the migration of the basal plate discontinuity and flow of clay. It then accommodates a component of divergence. Vertical dotted line shows the initial precut fault location. **e)** With additional displacement and new space created by extension (grey rectangle), the dip of the precut fault shallows further. A new secondary fault forms (red line) to accommodate extension in the hanging wall of the precut fault.

5.3.2 Left-Lateral Slip along Secondary Faults that Trend Parallel to the Releasing Segment

In addition to left-lateral slip along cross faults, the northwestern portions of secondary faults that strike subparallel to the releasing bend show instances of left-lateral slip in both experiments. For example, at

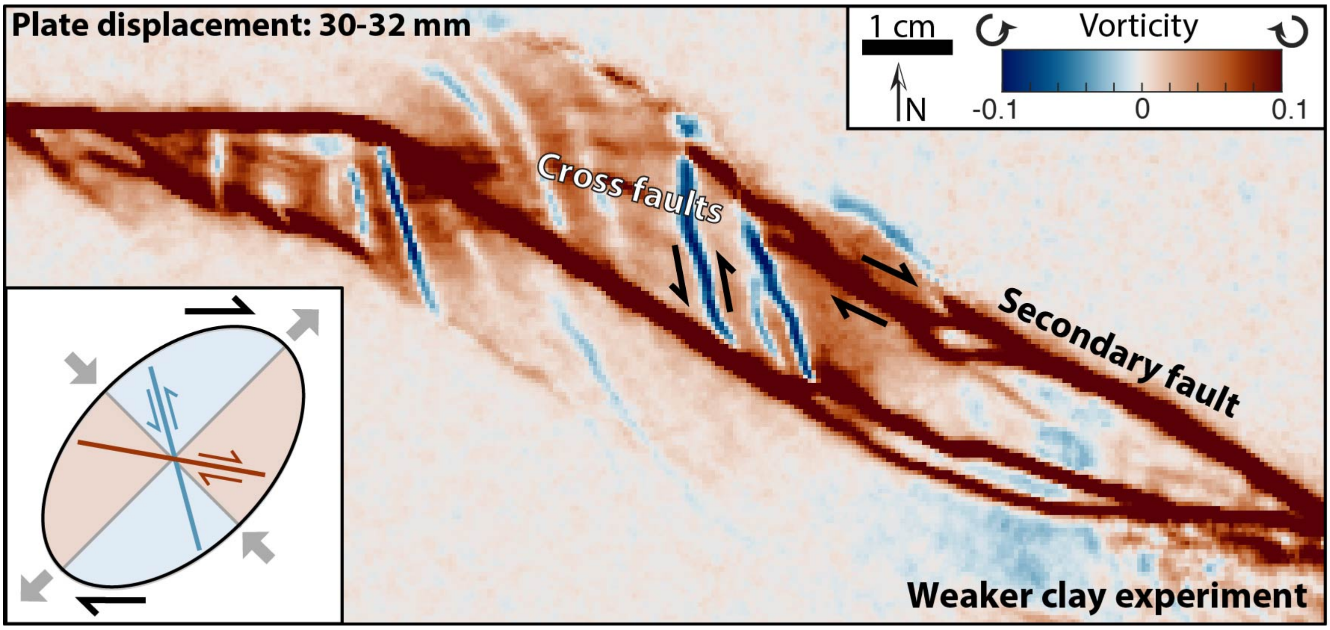

Figure 8 – Vorticity map at 30-32 mm of plate displacement for the weaker clay experiment. Red colors indicate clockwise rotation (right-lateral), and blue colors indicate counterclockwise rotation (left-lateral). Left-lateral cross faults develop between right-lateral faults. Inset shows schematic of instantaneous strain ellipse for right-lateral simple shear.

22-24 mm basal plate displacement, the incremental strain map for the stronger clay experiment shows left-lateral slip along the northwesterly portion of some secondary fault above the moving plate (Figure 9b). Faults in a similar orientation and position within the weaker clay experiment also show left-lateral slip.

The development of a component of left-lateral slip along northwest-southeast striking faults is not expected with the overall loading on the experiment and warrants closer investigation. Prior to secondary fault growth (8-10 mm plate displacement), the dilational map reveals two zones of overall extension that trend parallel to the releasing segment and outside of a strain shadow zone adjacent to the releasing bend segment (Figure 9a). With additional loading, the new normal faults developed within the two zones of extension (Figure 9c). The shear strain map prior to normal fault growth shows regions of right-lateral shear above the stationary plate and generally low shear strains above the moving plate (Figure 9b). The new secondary faults that grew above the stationary plate accommodated the previously distributed off-fault shear as right-lateral slip (Figure 9d).

The unexpected component of left-lateral slip along oblique slip secondary faults may arise from variations in normal fault strike. The fault segments that show left-lateral slip have a more north-south oriented trend than the segments with right-lateral slip. If we consider the idealized instantaneous strain ellipse for simple shear (inset Figure 8), faults trending more northerly than the 315° dashed lines on Figure 7d will host left-lateral slip. All the right-lateral faults in the experiment, including the segments of primary slip pathway trend more westerly than 315°. Because the secondary faults initiate as normal faults accommodating extension, their orientation is controlled by the pattern of early dilational strain (e.g., Figure 9a), that creates faults with a range of strikes, some of which are oriented to accommodate a component of left-lateral slip.

We are not aware of field observations of components of slip along normal faults adjacent to releasing bends that oppose the slip sense of overall loading. The opposite slip sense signal is subtle and may be difficult to detect within extensional landscapes subjected to active erosion and depositional processes.

5.4 Crustal Comparisons and Implications

We compare the pattern of faulting from this study's experiments to two crustal releasing bends with contrasting inferred crustal strengths due to differences in heat flow and crustal thickness: the Southern Gar Basin along the southern part of the Karakoram fault in Western Tibet and the Brawley Seismic Zone within the San Andreas fault system in southern California, USA (Figure 10). The Karakoram fault cuts thicker crust associated with convergence of the Himalaya and uplift of the Tibetan plateau (e.g., *Gilligan et al.*, 2015; *Priestley et al.*, 2008; *Rai et al.*, 2006). In contrast, The Brawley Seismic Zone is an area of notably hot and thin crust associated with nearby rifting of the Baja California Peninsula from mainland Mexico (e.g., *Elders et al.*, 1972; *Fuis et al.*, 1984; *Lachenbruch et al.*, 1985). Hot and thin crust, such as at the Brawley Seismic Zone, has lower overall strength than cooler, thicker continental crust, such as the Tibetian Plateau (e.g., *Lewis et al.*, 2003; *Molnar and Tapponnier*, 1981). The inferred strength of the crust differs between the two regions of complex faulting, and we consider these two releasing bends due to their similar geometries and strike-slip rates. Complex regional tectonics of the southern part of the Karakoram Fault system facilitated

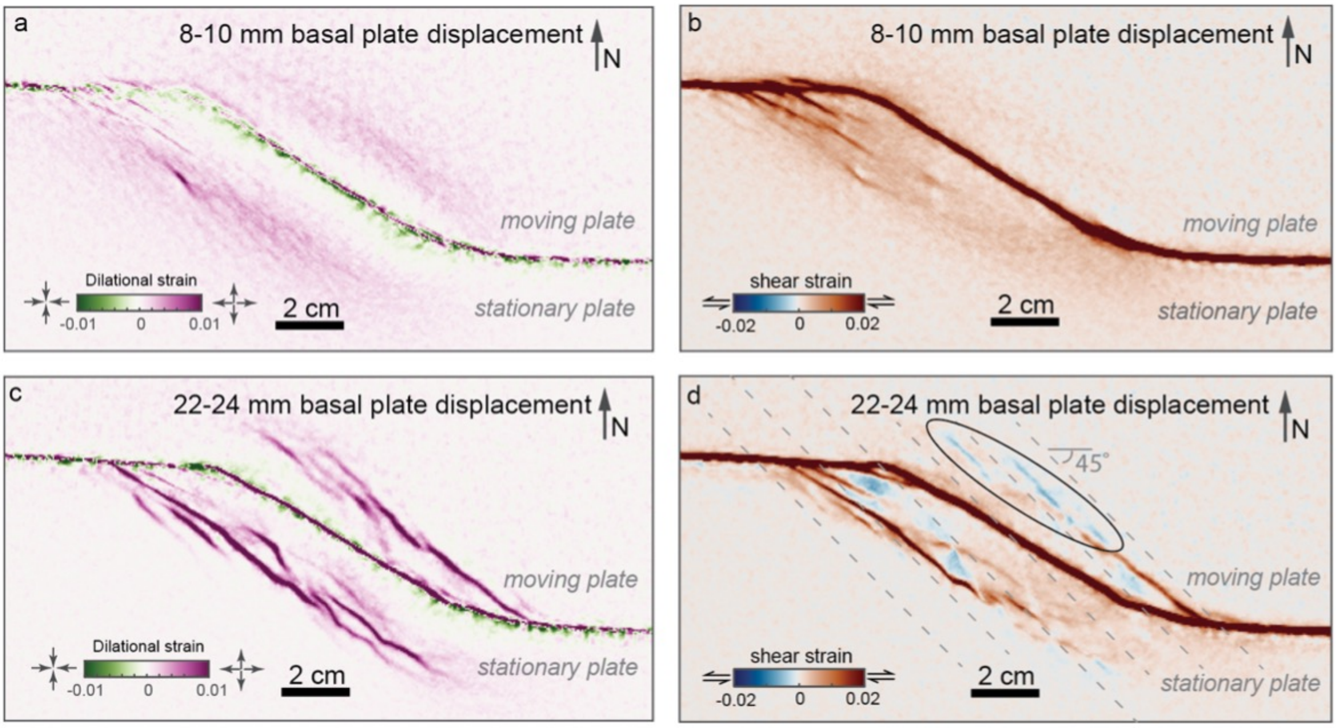

Figure 9 – Divergence and vorticity maps reveal the patterns of dilational and shear strain before **(a and b)** and after the growth of secondary faults **(c and d)** in the stronger clay experiment. Left-lateral slip emerges along the portion of the secondary faults distal to the primary slip pathway (ellipse on d) where faults have more north-south oriented strike than the faults with right-lateral slip. Dashed line at 45° degrees separates regions of left-lateral (>45°) and right lateral (<45°) conjugate faulting under an idealized instantaneous simple shear.

Table 2 – Features of Southern Gar Basin and Brawley Seismic Zone

	Offset angle	**Offset distance**	**Strike-slip rate**
Southern Gar Basin	20° (Figure 10a; *Sanchez et al.*, 2010)	9 km (Figure 10a; *Sanchez et al.*, 2010)	~5-11 mm/yr (1) (*Chevalier et al.*, 2012)
Brawley Seismic Zone	30° and 12° (2) (U.S. Geological Survey and California Geological Survey, 2020)	6 km (*Hauksson et al.*, 2022)	~17 mm/yr (3) (*Crowell et al.*, 2013)

(1) The strike-slip rate along the Karakoram fault just south of the Gar Basin and outside of the releasing bend is suggested to be in the range of 5-11 mm/yr (*Chevalier et al.*, 2012).

(2) The trend of the Brawley Seismic Zone diverged 30° and 12° to the main strike of the San Andreas Fault and the Imperial Fault respectively (U.S. Geological Survey and California Geological Survey, 2020).

(3) Geodetic estimates for opening (15 mm/yr) and strike slip (11 mm/yr) across Brawley Seismic Zone suggest a net strike-slip rate of 17 mm/yr parallel to the trend of San Andreas outside of the releasing bend (*Crowell et al.*, 2013).

the development of a double bend system in Gar Valley (*Lacassin et al.*, 2004), and here we focus on the Southern Gar Basin (Figure 10a). The Brawley Seismic Zone connects the San Andreas Fault in the north to the Imperial Fault to the south (Figure 10c). Instead of a single primary slip surface connecting the San Andreas and Imperial faults, this releasing bend has a zone of distributed strain and microseismicity (*Brothers et al.*, 2009). The differences in active fault patterns between the Brawley Seismic Zone and the Southern Gar Basin can be reasonably inferred to be due to differences in contrasting crustal strength because other influential characteristics (ie. fault geometry and strike-slip rates) are similar (Table 2).

The fault pattern in the Southern Gar Basin releasing bend resembles the pattern developed in the clay box experiments with stronger clay. For example, geologic evidence within the Southern Gar Basin suggests that the bend developed along a through-going strike-slip fault (*Sanchez et al.*, 2010) and changed from predominantly strike-slip to increased normal and oblique slip (*Lacassin et al.*, 2004). *Sanchez et al.* (2010) infer that the secondary normal faults of the southern Gar Basin changed dip during their evolution and originated with steeper dips than present. During releasing bend maturation within the past 13 Ma, new right-lateral normal faults developed subparallel to the primary releasing bend so that faults young basinward (*Sanchez et al.*, 2010). We note that fault maps do not show any active cross faults in the southern Gar Basin (Figure 10a). The releasing bend experiments within strong clay show many similar characteristics to the recent history of the releasing bend within the Southern Gar basin. For example, the dip of the precut releasing

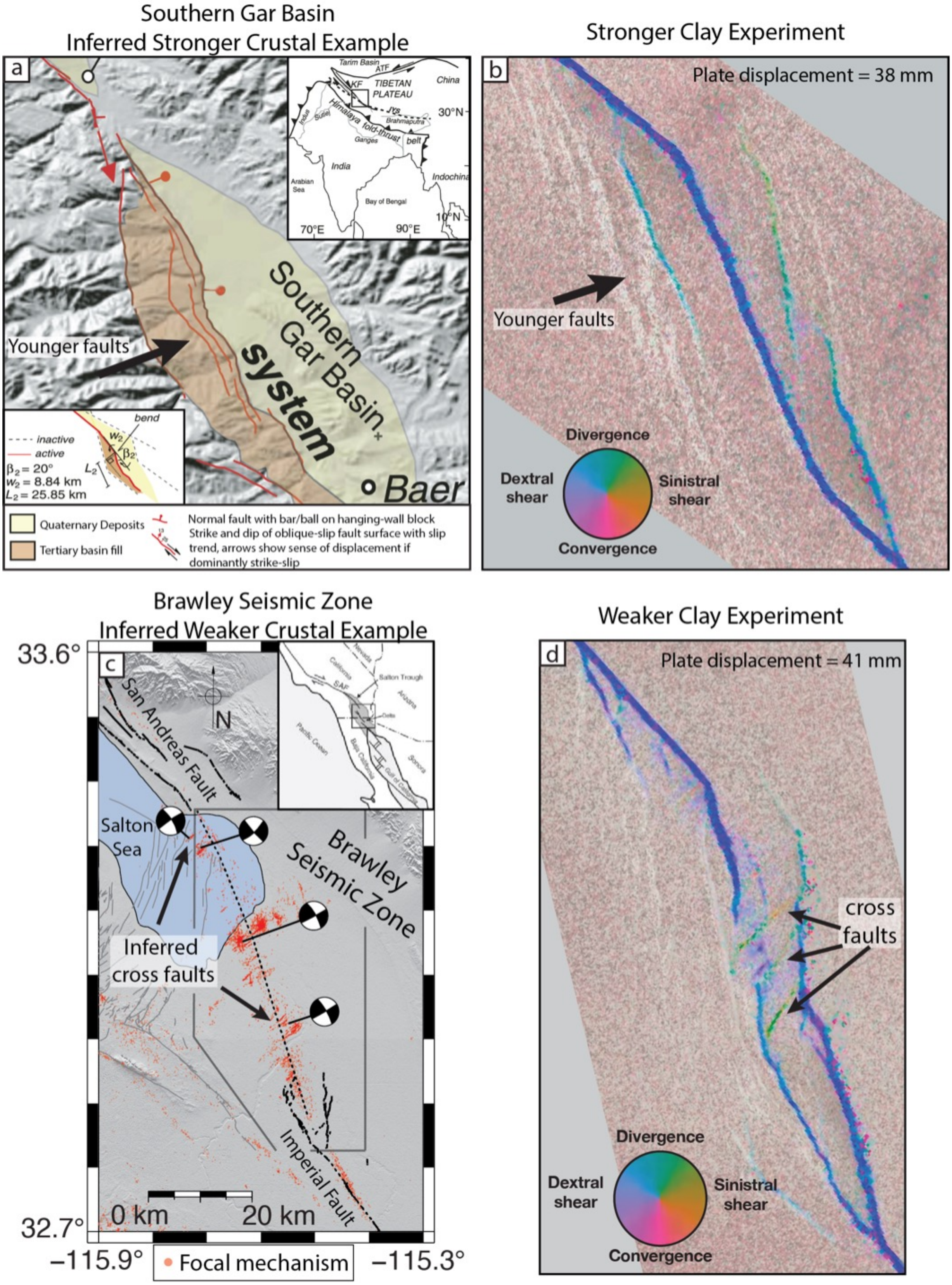

Figure 10 – **a)** Fault map of the Southern Gar Basin, Tibet modified from *Sanchez et al.* (2010). **b)** incremental strain map of the stronger clay experiment at 38 mm of plate displacement showing normal slip along secondary faults. **c)** Active faults from the USGS Quaternary Fault and Fold Database and focal mechanism locations (*Yang et al.*, 2012) in the Brawley Seismic Zone, USA. The dotted black line represents the diffuse zone of faulting withing the Brawley Seismic zone. Grey faults are those with slip rates <5 mm/yr. Black faults are the primary releasing bend structures and slip rates >5 mm/yr. For example, focal mechanisms highlight slip on potential cross faults. Inset modified from *Meltzner et al.* (2006). **d)** Incremental strain map of the weaker clay experiment at 41 mm plate displacement. Hue shows slip sense while intensity reveals rate.

bend segment shallows over the course of the experiment, which we interpret as resulting from basinward lateral flow at depth. Within the stronger clay experiment, secondary normal faults also young basinward (most notable during stage 1 (Figure 3; Figure 10b) similarly to the normal faults of the southern Gar Basin. Overall, the stronger claybox experiment exhibits a similar degree of complexity and localized faulting as the Gar Basin in terms of the numbers of and orientation of secondary faults that develop around the releasing bend. Lastly, the stronger clay experiment does not show the development of abundant cross faults, which is also consistent with observed faulting in the southern Gar basin.

The fault structures of the Brawley Seismic Zone have many similarities to those that develop within the weaker clay experiment. While the active fault map for the releasing bend shows a continuous fault trace that connects the San Andreas and Imperial faults, this is a simplified representation, and seismicity reveals that slip is distributed across hundreds of faults within this zone. Seismicity within the releasing bend of the Brawley Seismic Zone reveals an intricate pattern of subparallel north-south trending right-lateral faults and northeast-southwest trending left-lateral faults (Figure 10c). The weaker clay experiment also developed many cross faults that have slip sense opposite to the right-lateral primary faults. While the weaker clay experiment produced fewer active slip surfaces than the Brawley Seismic Zone, they both host a similar pattern of distributed conjugate faulting.

Both the similarities between the experiments of different material strength and their crustal counterparts as well as the major differences between the stronger and weaker experiments showcase the applicability of the scaled physical experiments to the study of faulting within regions of different crustal strength. From these comparisons, we can infer that releasing bends within stronger crust, such as thicker and cooler crust, will develop localized faulting that is more persistent over time than releasing bends within areas of weaker crust that might be thinner and warmer.

The degree of fault localization or delocalization within releasing bends impacts seismic hazards. For example, for regions of similar tectonic loading, releasing bends in stronger material will have more localized fault systems with greater slip rates along active fault, which increases the potential for larger magnitude earthquakes. Fault slip rate is a primary factor in seismic hazard assessment (e.g., *Hatem et al.*, 2022). Increased seismic hazard with fault localization could have implications for regions of strong crust like the Southern Gar Basin. On the other hand, as seen in the weaker clay experiment, many faults may be concurrently active when faulting is delocalized. While the distribution of strain along many faults reduces slip rate, this delocalization also increases the potential for occurrence of complex multi-segment ruptures whose details are difficult to anticipate (e.g., *Cesca et al.*, 2017; *Hollingsworth et al.*, 2017; *Ross et al.*, 2019). For example, damaging earthquakes within the Brawley Seismic Zone may rupture along many potential fault surfaces making it challenging to consider hazard locations (*Hauksson et al.*, 2022). Additionally, multi-segment ruptures within delocalized fault systems can produce abundant off-fault deformation (e.g., *Milliner et al.*, 2021; *Zinke et al.*, 2019) including landslides (e.g., *Bloom et al.*, 2022), which has significant impact on safety and infrastructure. While many factors contribute to seismic hazard at releasing bends, the experiments of this study shed light on the impact of material strength on localization and complexity of active fault patterns that impact seismic hazard.

6 Conclusions

This study investigates the impact of material strength on the degree of fault localization, number of active faults and off-fault deformation that develop at releasing bends along strike-slip faults. Scaled physical experiments of releasing bends that use clay as an analog for crustal materials show that weaker clay facilitates the growth of a greater number of secondary normal faults, the development of left-lateral cross faults and greater off-fault deformation. The delocalized nature of faulting within the weak clay experiment also contributes to major reorganization of the primary slip pathway through the releasing bend. Stronger clay inhibits the development of cross faults and major reorganization of the primary slip path and develops lesser off-fault deformation. The stronger clay experiment produces a more localized fault network with a more persistent fault geometry than in weaker clay. In both experimental fault systems, portions of secondary faults have left-lateral slip within the overall right-lateral system. Both experiments also show shallowing dip of the vertical precut faults facilitated by lateral flow of clay at depth.

This experimental study is effectively able to isolate the impact material strength has on releasing bend fault evolution and allows for direct observation of the entire fault evolution. The characteristics of faults within the analog experiments (i.e., localization, persistence, pattern and evolution) resemble those of crustal releasing bends of differing crustal strength due to different heat flux and crustal thickness at the Brawley Seismic Zone, USA and the Southern Gar Basin, Tibet. Consequently, the insights into releasing bend fault evolution from these scaled physical experiments can provide guidance on other crustal regions with relatively strong (thick and cool) or weak (thin and hot) crust.

Acknowledgements

This research was supported by grant EAR 2040570 from the National Science Foundation. We thank Jürgen Adam, Tim Dooley, Jakub Fedorik, and an anonymous reviewer for their thoughtful feedback and suggestions.

Author contributions

A. Gabriel led the experiments with help from **H. Elston** and **C. Ramos Sánchez**. **C. Ramos Sánchez**

performed the Structure from Motion data collection and analysis. **A. Gabriel** led the data analysis with help from **H. Elston** and **M. Cooke**. All authors were involved in the writing and revising of the manuscript.

Data availability

The experimental data, including both incremental horizontal displacements and elevation maps are available at the European Plate Observing System (EPOS) data repository for analog experiments. Strain animations from all four experiments are also available in *Gabriel et al.* (2025).

Competing interests

The authors declare no competing interests.

Peer review

This publication was peer-reviewed by Jürgen Adam, Tim Dooley, Jakub Fedorik, and an anonymous reviewer. The full peer-review report can be found here: Review Report.

Copyright notice

References

Adam, J., J. L. Urai, B. Wieneke, O. Oncken, K. Pfeiffer, N. Kukowski, J. Lohrmann, S. Hoth, W. van der Zee, and J. Schmatz (2005), Shear localisation and strain distribution during tectonic faulting—new insights from granular-flow experiments and high-resolution optical image correlation techniques, *Journal of structural geology*, *27*(2), 283–301, doi: 10.1016/j.jsg.2004.08.008.

Barka, A. A., and K. Kadinsky-Cade (1988), Strike-slip fault geometry in Turkey and its influence on earthquake activity, *Tectonics*, *7*(3), 663–684, doi: 10.1029/tc007i003p00663.

Biasi, G. P., and S. G. Wesnousky (2016), Steps and gaps in ground ruptures: Empirical bounds on rupture propagation, *Bulletin of the Seismological Society of America*, *106*(3), 1110–1124, doi: 10.1785/0120150175.

Biasi, G. P., and S. G. Wesnousky (2017), Bends and ends of surface ruptures, *Bulletin of the Seismological Society of America*, *107*(6), 2543–2560, doi: 10.1785/0120160292.

Bloom, C. K., A. Howell, T. Stahl, C. Massey, and C. Singeisen (2022), The influence of off-fault deformation zones on the near-fault distribution of coseismic landslides, *Geology*, *50*(3), 272–277, doi: 10.1130/g49429.1.

Bonali, F. L., A. Tibaldi, F. Marchese, L. Fallati, E. Russo, C. Corselli, and A. Savini (2019), UAV-based surveying in volcano-tectonics: An example from the Iceland rift, *Journal of structural geology*, *121*, 46–64, doi: 10.1016/j.jsg.2019.02.004.

Bonini, L., R. Basili, G. Toscani, P. Burrato, S. Seno, and G. Valensise (2016), The effects of pre-existing discontinuities on the surface expression of normal faults: Insights from wet-clay analog modeling, *Tectonophysics*, *684*, 157–175, doi: 10.1016/J.TECTO.2015.12.015.

Bonini, L., U. Fracassi, N. Bertone, F. E. Maesano, G. Valensise, and R. Basili (2023), How do inherited dip-slip faults affect the development of new extensional faults? Insights from wet clay analog models, *Journal of structural geology*, *169*(104836), 104,836, doi: 10.1016/j.jsg.2023.104836.

Brothers, D. S., N. W. Driscoll, G. M. Kent, A. J. Harding, J. M. Babcock, and R. L. Baskin (2009), Tectonic evolution of the Salton Sea inferred from seismic reflection data, *Nature geoscience*, *2*(8), 581–584, doi: 10.1038/ngeo590.

Cesca, S., Y. Zhang, V. Mouslopoulou, R. Wang, J. Saul, M. Savage, S. Heimann, S.-K. Kufner, O. Oncken, and T. Dahm (2017), Complex rupture process of the Mw 7.8, 2016, Kaikoura earthquake, New Zealand, and its aftershock sequence, *Earth and planetary science letters*, *478*, 110–120, doi: 10.1016/j.epsl.2017.08.024.

Chaipornkaew, L., H. Elston, M. Cooke, T. Mukerji, and S. A. Graham (2022), Predicting off-fault deformation from experimental strike-slip fault images using convolutional neural networks, *Geophysical research letters*, *49*(2), doi: 10.1029/2021gl096854.

Chevalier, M.-L., P. Tapponnier, J. Van der Woerd, F. J. Ryerson, R. C. Finkel, and H. Li (2012), Spatially constant slip rate along the southern segment of the Karakorum fault since 200ka, *Tectonophysics*, *530-531*, 152–179, doi: 10.1016/j.tecto.2011.12.014.

Choi, E., L. Seeber, M. S. Steckler, and R. Buck (2011), One-sided transform basins and "inverted curtains": Implications for releasing bends along strike-slip faults: ONE-SIDED TRANSFORM BASINS, *Tectonics*, *30*(6), doi: 10.1029/2011tc002943.

Cooke, M. L., and N. J. van der Elst (2012), Rheologic testing of wet kaolin reveals frictional and bi-viscous behavior typical of crustal materials: RHEOLOGIC TESTING OF WET KAOLIN, *Geophysical research letters*, *39*(1), 2011GL050,186, doi: 10.1029/2011gl050186.

Cooke, M. L., M. T. Schottenfeld, and S. W. Buchanan (2013), Evolution of fault efficiency at restraining bends within wet kaolin analog experiments, *Journal of Structural Geology*, *51*, 180–192, doi: 10.1016/j.jsg.2013.01.010.

Crowell, B. W., Y. Bock, D. T. Sandwell, and Y. Fialko (2013), Geodetic investigation into the deformation of the Salton Trough: DEFORMATION OF THE SALTON TROUGH, *Journal of geophysical research. Solid earth*, *118*(9), 5030–5039, doi: 10.1002/jgrb.50347.

DeGroot, D. J., and T. Lunne (2007), Measurement of Remoulded Shear Strength, *Tech. Rep. 20061023-1*, Norwegian Geotechnical Institute.

DeLong, S. B., J. J. Lienkaemper, A. J. Pickering, and N. N. Avdievitch (2015), Rates and patterns of surface deformation from laser scanning following the South Napa earthquake, California, *Geosphere*, *11*(6), 2015–2030, doi: 10.1130/GES01189.1.

Dooley, T., and K. McClay (1997), Analog modeling of pull-apart basins, *AAPG bulletin*, *81*, doi: 10.1306/3b05c636-172a-11d7-8645000102c1865d.

Dooley, T., K. McClay, and M. Bonora (1999), 4D evolution of segmented strike-slip fault systems: applications to

NW Europe, in *Petroleum Geology of Northwest Europe: Proceedings of the 5th Conference*, vol. 5, pp. 215–225, Geological Society of London, doi: 10.1144/0050215.

Dooley, T. P., and G. Schreurs (2012), Analogue modelling of intraplate strike-slip tectonics: A review and new experimental results, *Tectonophysics*, *574-575*, 1–71, doi: 10.1016/j.tecto.2012.05.030.

Douilly, R. (2023), Effect of asymmetric topography on rupture propagation along fault stepovers, *Journal of geophysical research. Solid earth*, *128*(7), e2023JB026,484, doi: 10.1029/2023jb026484.

Duffy, B., M. Quigley, D. J. A. Barrell, R. Van Dissen, T. Stahl, S. Leprince, C. McInnes, and E. Bilderback (2013), Fault kinematics and surface deformation across a releasing bend during the 2010 MW 7.1 Darfield, New Zealand, earthquake revealed by differential LiDAR and cadastral surveying, *Geological Society of America bulletin*, *125*(3-4), 420–431, doi: 10.1130/B30753.1.

Eisenstadt, G., and D. Sims (2005), Evaluating sand and clay models: do rheological differences matter?, *Journal of structural geology*, *27*(8), 1399–1412, doi: 10.1016/j.jsg.2005.04.010.

Elders, W. A., R. W. Rex, P. T. Robinson, S. Biehler, and T. Meidav (1972), Crustal Spreading in Southern California: The Imperial Valley and the Gulf of California formed by the rifting apart of a continental plate: The Imperial Valley and the Gulf of California formed by the rifting apart of a continental plate, *Science (New York, N.Y.)*, *178*(4056), 15–24, doi: 10.1126/science.178.4056.15.

Elston, H., M. Cooke, and A. Hatem (2022), Non-steady-state slip rates emerge along evolving restraining bends under constant loading, *Geology*, *50*(5), 532–536, doi: 10.1130/g49745.1.

Fuis, G. S., W. D. Mooney, J. H. Healy, G. A. McMechan, and W. J. Lutter (1984), A seismic refraction survey of the Imperial Valley Region, California, *Journal of geophysical research*, *89*(B2), 1165–1189, doi: 10.1029/jb089ib02p01165.

Gabriel, A., H. Elston, M. Cooke, and C. Ramos Sanchez (2025), Digital Image Correlation data from experiments of releasing bend evolution within different strength wet kaolin. GFZ Data Services, doi: 10.5880/fidgeo.2024.015.

Galland, O., H. S. Bertelsen, F. Guldstrand, L. Girod, R. F. Johannessen, F. Bjugger, S. Burchardt, and K. Mair (2016), Application of open-source photogrammetric software MicMac for monitoring surface deformation in laboratory models, *Journal of geophysical research. Solid earth*, *121*(4), 2852–2872, doi: 10.1002/2015jb012564.

Gilligan, A., K. F. Priestley, S. W. Roecker, V. Levin, and S. S. Rai (2015), The crustal structure of the western Himalayas and Tibet: CRUSTAL STRUCTURE ACROSS W. TIBET, *Journal of geophysical research. Solid earth*, *120*(5), 3946–3964, doi: 10.1002/2015jb011891.

Graymer, R. W., V. E. Langenheim, R. W. Simpson, R. C. Jachens, and D. A. Ponce (2007), Relatively simple through-going fault planes at large-earthquake depth may be concealed by the surface complexity of strike-slip faults, *Geological Society special publication*, *290*(1), 189–201, doi: 10.1144/sp290.5.

Hatem, A. E., M. L. Cooke, and E. H. Madden (2015), Evolving efficiency of restraining bends within wet kaolin analog experiments, *Journal of geophysical research. Solid earth*, *120*(3), 1975–1992, doi: 10.1002/2014jb011735.

Hatem, A. E., M. L. Cooke, and K. Toeneboehn (2017), Strain localization and evolving kinematic efficiency of initiating strike-slip faults within wet kaolin experiments, *Journal of structural geology*, *101*, 96–108, doi: 10.1016/j.jsg.2017.06.011.

Hatem, A. E., N. G. Reitman, R. W. Briggs, R. D. Gold, J. A. Thompson Jobe, and R. J. Burgette (2022), Western U.s. geologic deformation model for use in the U.s. national Seismic Hazard Model 2023, *Seismological research letters*, *93*(6), 3053–3067, doi: 10.1785/0220220154.

Hauksson, E., J. M. Stock, and A. L. Husker (2022), Seismicity in a weak crust: the transtensional tectonics of the Brawley Seismic Zone section of the Pacific–North America Plate Boundary in Southern California, USA, *Geophysical journal international*, *231*(1), 717–735, doi: 10.1093/gji/ggac205.

Hempton, M. R., and K. Neher (1986), Experimental fracture, strain and subsidence patterns over en échelon strike-slip faults: implications for the structural evolution of pull-apart basins, *Journal of structural geology*, *8*(6), 597–605, doi: 10.1016/0191-8141(86)90066-0.

Henza, A. A., M. O. Withjack, and R. W. Schlische (2010), Normal-fault development during two phases of non-coaxial extension: An experimental study, *Journal of structural geology*, *32*(11), 1656–1667, doi: 10.1016/j.jsg.2009.07.007.

Hollingsworth, J., L. Ye, and J.-P. Avouac (2017), Dynamically triggered slip on a splay fault in the M_w 7.8, 2016 Kaikoura (New Zealand) earthquake: Mw7.8, 2016 Kaikoura Earthquake, *Geophysical research letters*, *44*(8), 3517–3525, doi: 10.1002/2016gl072228.

Hubbert, M. K. (1937), Theory of scale models as applied to the study of geologic structures, *Geological Society of America bulletin*, *48*(10), 1459–1520, doi: 10.1130/GSAB-48-1459.

Lacassin, R., F. Valli, N. Arnaud, P. H. Leloup, J. L. Paquette, L. Haibing, P. Tapponnier, M.-L. Chevalier, S. Guillot, G. Maheo, and X. Zhiqin (2004), Large-scale geometry, offset and kinematic evolution of the Karakorum fault, Tibet, *Earth and planetary science letters*, *219*(3-4), 255–269, doi: 10.1016/s0012-821x(04)00006-8.

Lachenbruch, A. H., J. H. Sass, and S. P. Galanis (1985), Heat flow in southernmost California and the origin of the Salton Trough, *Journal of geophysical research*, *90*(B8), 6709–6736, doi: 10.1029/JB090iB08p06709.

Lewis, T. J., R. D. Hyndman, and P. Flück (2003), Heat flow, heat generation, and crustal temperatures in the northern Canadian Cordillera: Thermal control of tectonics, *Journal of geophysical research*, *108*(B6), 2002JB002,090, doi: 10.1029/2002JB002090.

Mann, P. (2007), Global catalogue, classification and tectonic origins of restraining- and releasing bends on active and ancient strike-slip fault systems, *Geological Society special publication*, *290*(1), 13–142, doi: 10.1144/sp290.2.

Meltzner, A. J., T. K. Rockwell, and L. A. Owen (2006), Recent and long-term behavior of the Brawley fault zone, imperial valley, California: An escalation in slip rate?, *Bulletin of the Seismological Society of America*, *96*(6), 2304–2328, doi: 10.1785/0120050233.

Milliner, C., A. Donnellan, S. Aati, J.-P. Avouac, R. Zinke, J. F. Dolan, K. Wang, and R. Bürgmann (2021), Bookshelf kinematics and the effect of dilatation on fault zone inelastic deformation: Examples from optical image correlation measurements of the 2019 Ridgecrest earthquake sequence, *Journal of geophysical* *research. Solid earth*, *126*(3), e2020JB020,551, doi: 10.1029/2020jb020551.

Mitra, S., and D. Paul (2011), Structural geometry and evolution of releasing and restraining bends: Insights from laser-scanned experimental models, *AAPG bulletin*, *95*(7), 1147–1180, doi: 10.1306/09271010060.

Molnar, P., and P. Tapponnier (1981), A possible dependence of tectonic strength on the age of the crust in Asia, *Earth and planetary science letters*, *52*(1), 107–114, doi: 10.1016/0012-821x(81)90213-2.

Nixon, C. W., D. J. Sanderson, and J. M. Bull (2011), Deformation within a strike-slip fault network at Westward Ho!, Devon U.K.: Domino vs conjugate faulting, *Journal of structural geology*, *33*(5), 833–843, doi: 10.1016/j.jsg.2011.03.009.

Ozawa, S., R. Ando, and E. M. Dunham (2023), Quantifying the probability of rupture arrest at restraining and releasing bends using earthquake sequence simulations, *Earth and planetary science letters*, *617*(118276), 118,276, doi: 10.1016/j.epsl.2023.118276.

Priestley, K., J. Jackson, and D. McKenzie (2008), Lithospheric structure and deep earthquakes beneath India, the Himalaya and southern Tibet, *Geophysical journal international*, *172*(1), 345–362, doi: 10.1111/j.1365-246X.2007.03636.x.

Rahe, B., D. A. Ferrill, and A. P. Morris (1998), Physical analog modeling of pull-apart basin evolution, *Tectonophysics*, *285*(1-2), 21–40, doi: 10.1016/s0040-1951(97)00193-5.

Rai, S. S., K. Priestley, V. K. Gaur, S. Mitra, M. P. Singh, and M. Searle (2006), Configuration of the Indian Moho beneath the NW Himalaya and Ladakh, *Geophysical research letters*, *33*(15), L15,308, doi: 10.1029/2006GL026076.

Reber, J. E., M. L. Cooke, and T. P. Dooley (2020), What model material to use? A Review on rock analogs for structural geology and tectonics, *Earth-science reviews*, *202*(103107), 103,107, doi: 10.1016/j.earscirev.2020.103107.

Ross, Z. E., B. Idini, Z. Jia, O. L. Stephenson, M. Zhong, X. Wang, Z. Zhan, M. Simons, E. J. Fielding, S.-H. Yun, E. Hauksson, A. W. Moore, Z. Liu, and J. Jung (2019), Hierarchical interlocked orthogonal faulting in the 2019 Ridgecrest earthquake sequence, *Science (New York, N.Y.)*, *366*(6463), 346–351, doi: 10.1126/science.aaz0109.

Sanchez, V. I., M. A. Murphy, W. R. Dupre, L. Ding, and R. Zhang (2010), Structural evolution of the Neogene Gar Basin, western Tibet: Implications for releasing bend development and drainage patterns, *Geological Society of America bulletin*, *122*(5-6), 926–945, doi: 10.1130/B26566.1.

Sylvester, A. G. (1988), Strike-slip faults, *Geological Society of America bulletin*, *100*(11), 1666–1703, doi: 10.1130/0016-7606(1988)100<1666:SSF>2.3.CO;2.

Thielicke, W., and R. Sonntag (2021), Particle Image Velocimetry for MATLAB: Accuracy and enhanced algorithms in PIVlab, *Journal of open research software*, *9*(1), 12, doi: 10.5334/jors.334.

van Wijk, J., G. Axen, and R. Abera (2017), Initiation, evolution and extinction of pull-apart basins: Implications for opening of the Gulf of California, *Tectonophysics*, *719-720*, 37–50, doi: 10.1016/j.tecto.2017.04.019.

von Hagke, C., M. Kettermann, N. Bitsch, D. Bücken, C. Weismüller, and J. L. Urai (2019), The effect of obliquity of slip in normal faults on distribution of open fractures, *Frontiers in earth science*, *7*, 18, doi: 10.3389/feart.2019.00018.

Wang, H., M. Liu, J. Ye, J. Cao, and Y. Jing (2017), Strain partitioning and stress perturbation around stepovers and bends of strike-slip faults: Numerical results, *Tectonophysics*, *721*, 211–226, doi: 10.1016/j.tecto.2017.10.001.

Wang, H., M. Liu, B. Duan, and J. Cao (2020), Rupture propagation along stepovers of strike-slip faults: Effects of initial stress and fault geometry, *Bulletin of the Seismological Society of America*, *110*(3), 1011–1024, doi: 10.1785/0120190233.

Wesnousky, S. G. (2006), Predicting the endpoints of earthquake ruptures, *Nature*, *444*(7117), 358–360, doi: 10.1038/nature05275.

Withjack, M., and R. Schlische (2006), Geometric and experimental models of extensional fault-bend folds, *Geological Society special publication*, *253*(1), 285–305, doi: 10.1144/GSL.SP.2006.253.01.15.

Withjack, M. O., and W. R. Jamison (1986), Deformation produced by oblique rifting, *Tectonophysics*, *126*(2-4), 99–124, doi: 10.1016/0040-1951(86)90222-2.

Wu, J. E., K. McClay, P. Whitehouse, and T. Dooley (2009), 4D analogue modelling of transtensional pull-apart basins, *Marine and petroleum geology*, *26*(8), 1608–1623, doi: 10.1016/j.marpetgeo.2008.06.007.

Xu, H., H. Lao, C. Peng, H. Xu, C. Liu, W. Sun, Y. Ju, and G. Dong (2023), Reacquainting the structural characteristics of pull-apart basins based on simulations with wet clay, *Sustainability*, *15*(19), 14,143, doi: 10.3390/su151914143.

Yang, W., E. Hauksson, and P. Shearer (2012), Computing a large refined catalog of focal mechanisms for southern California (1981-2010): Temporal stability of the style of faulting, *Bulletin of the Seismological Society of America*, *102*(3), 1179–1194, doi: 10.1785/0120110311.

Zinke, R., J. Hollingsworth, J. F. Dolan, and R. Van Dissen (2019), Three-dimensional surface deformation in the 2016 M7.8 Kaikōura, New Zealand, earthquake from optical image correlation: Implications for strain localization and long-term evolution of the pacific-Australian plate boundary, *Geochemistry, geophysics, geosystems: G(3)*, *20*(3), 1609–1628, doi: 10.1029/2018gc007951.